EUROFUSION WP15ER-PR(15) 14493

R. Pasquetti et al.

# Fourier-spectral element approximation of the ion-electron Braginskii system with application to tokamak edge plasma in divertor configuration

Preprint of Paper to be submitted for publication in
Journal of Computational Physics

This work has been carried out within the framework of the EUROfusion Consortium and has received funding from the Euratom research and training programme 2014-2018 under grant agreement No 633053. The views and opinions expressed herein do not necessarily reflect those of the European Commission.

# Fourier-spectral element approximation of the ion-electron Braginskii system with application to tokamak edge plasma in divertor configuration

Sebastian Minjeaud and Richard Pasquetti[1]

*Lab. J. A. Dieudonné, UMR CNRS 7351, Université de Nice-Sophia Antipolis, F-06108 Nice, France & INRIA project CASTOR.*

**Abstract**

Due to the extreme conditions required to produce energy by nuclear fusion in tokamaks, simulating the plasma behavior is an important but challenging task. We focus on the edge part of the plasma, where fluid approaches are probably the best suited, and our approach relies on the full Braginskii ion-electron model. This results in a set of 10 strongly coupled and non-linear conservation equations that exhibit multiscale and anisotropy features. They are solved in a torus of complex geometrical section, that corresponds to the divertor configuration, *i.e.* with an "X-point" in the magnetic surfaces. To capture the complex physics that is involved, high order methods are used: The time-discretization is based on a Strang splitting, that combines implicit and explicit high order Runge-Kutta schemes, and the space discretization makes use of the spectral element method in the poloidal plane together with Fourier expansions in the toroidal direction. The paper describes the algorithms that have been developed and provides the results of preliminary numerical experiments.

*Keywords:*
Magnetic confined fusion; Edge plasma; Braginskii closures; High order methods.

## 1. Introduction

Although the first investigations on magnetic confined fusion trace back to the early 50's, in Russia, researches on this topic remain of strong actuality with the present construction in Cadarache of the ITER tokamak. Thus, important efforts about the numerical simulation of the plasma behavior are worldwide carried out, and many models are used depending on the part of the plasma which is considered (the core or the edge), on the time scale which is focused on or on the particular objective which is aimed at. Among the modeling strategies, one may essentially discern kinetic (or gyrokinetic), multi-fluid, magnetohydrodynamic (MHD) or Grad-Shafranov approaches, see *e.g.* [23] and references herein. For instance, a direct numerical simulation, see *e.g.* [19], needs a more accurate description of the evolution of the plasma than the one required for control considerations, see *e.g.* [6].

Because we are interested in short time scale turbulence phenomena in the scrape off layer (SOL), *i.e.* in the edge part of the plasma, the approach that we consider relies on the multi-fluid model that results from the moments of the Boltzmann equation expressed for the ions and the electrons, together with Braginskii like closures, as generally obtained using the Chapman-Enskog methodology [3, 9, 21, 29]. Fluid approaches are here relevant, because the temperature in the SOL is less high, *i.e.* generally of order of millions of degrees rather than hundreds of millions in the core, and also since the geometry may be much more complex. At this point, several variants are possible, leading to the MHD equations [1, 15, 28] or to multi-fluid equations, and several simplifications are conceivable. For instance, in the codes BOUT, GBS or TOKAM3X [12, 33, 36], the so-called drift velocity approximation is used. It mainly consists in solving only for the components, of

[1]Corresponding author. E-mail address: richard.pasquetti@unice.fr

the ion and electron velocities, that are parallel to the magnetic field, thus allowing a drastic reduction in the number of unknowns. Other approaches, based on further simplifications of the physical model are also possible, see *e.g.* [4, 5, 32].

Like in [25, 34], we do not use the velocity drift approximation, in order to rely on a more relevant model to describe plasma turbulence phenomena and also to provide a different and so complementary approach to more usual investigations. In a first step, we only consider electrically charged particles, *i.e.* the ions and the electrons, but a fluid modeling of neutral particles could be rather easily implemented in this framework. We also assume that at the short time-scales that we consider, the magnetic fluctuations can be neglected.

The resulting set of partial differential equations (PDEs) is solved using a high order numerical method in view to capture the instabilities that may develop in the plasma. Our numerical approach combines Fourier expansions in the toroidal direction with a spectral element method (SEM) in the poloidal plane. Using Fourier expansions more or less allows to address a set of two-dimensional problems rather the 3D one. The SEM is essentially a high order finite element method, that makes use in its 2D native form of unstructured quadrangular meshes, and of the tensorial product of Lagrange polynomials based on the Gauss-Lobatto-Legendre nodes, so that interpolation and quadrature points coincide [10, 17, 24]. The SEM approximation is well adapted to the complex geometries that are met when considering a tokamak in divertor configuration. Such a configuration is indeed characterized by the presence of an "X point" on the magnetic line (called the separatrix) that separates the closed and the open magnetic lines.

In Section 2, we go into the details of the physical model and outline the expected numerical difficulties. In Section 3, we describe the numerical method, which should be able to handle strongly anisotropic non self adjoint problems and also to support severe constraints on the time-step. In Section 4, we define the initial and boundary conditions of the problem that we want to address, and especially focus on the non-trivial so-called Bohm condition that should be enforced at the plates. Numerical results are provided and discussed. We conclude in Section 5.

## 2. The physical model

The physical model is essentially a two-fluid ion-electron model as may obtained from the moments of the Boltzmann equation together with the Braginskii closures. The physical assumptions we make to obtain this system of PDEs are given in Section 2.1. The complete set of equations is presented in Section 2.2, whereas the Braginskii closures are recalled in Section 2.3. Finally, in Section 2.4, we describe some of the difficulties associated to the present model.

### *2.1. Framework and physical assumptions*

The modeling relies on the following assumptions:

(i) A two-fluid ion-electron modeling, based on the equations of conservation of density, momentum and energy for each species, together with the Braginskii closures, is relevant.
(ii) The plasma is electrically neutral: $\sum_s n_s e_s = 0$ ($n_s$: species density, $e_s$: species charge, $s = \{i, e\}$).
(iii) The magnetic field $\boldsymbol{B}$ is axisymmetric and its fluctuations in time are negligible with respect to the magnetic field imposed by the coils.
(iv) The electric field is electrostatic: $\boldsymbol{E} = -\nabla U$ ($\boldsymbol{E}$: electric field, $U$: electric potential).
(v) The species temperature $T_s$ and pressure $p_s$ are linked by state laws of the form $p_s = n_s T_s$ and one has $\varepsilon_s = p_s/(\gamma - 1)$ ($\varepsilon_s$: internal energy, $\gamma$: ratio of specific heats).

Note that the assumptions (iii) and (iv) are coherent with the Maxwell-Faraday equation : $\nabla \times \boldsymbol{E} = -\partial_t \boldsymbol{B}$. More precisely, the assumption (iv) may be deduced from the assumption (iii) and the Maxwell-Faraday equation since they give: $\nabla \times \boldsymbol{E} = 0$.

In addition to the coupling due to the Braginskii closures, the assumptions (ii) and (iv) induce a strong coupling between the conservation equations for ions and for electrons. The electric potential $U$ may be seen

as a additional unknown associated to the constraint of electric neutrality, which translates into a divergence free constraint on the current. Indeed, using the particles conservation equations:

$$\partial_t n_s + \nabla \cdot (n_s \boldsymbol{u}_s) = 0, \tag{1}$$

where $\boldsymbol{u}_s$ is the species velocity, by first multiplying the ion and the electron conservation equation by the ion and electron electric charge, respectively, and then summing, one finds that ensuring the electroneutrality is equivalent to ensure that the current, $\boldsymbol{j} = \sum_s n_s e_s \boldsymbol{u}_s$, is divergence free: $\nabla \cdot \boldsymbol{j} = 0$.

*2.2. The complete set of equations*

Let us now define the species mass densities $\rho_s = n_s m_s$ ($m_s$: species mass), the species momentums $\boldsymbol{q}_s = \rho_s \boldsymbol{u}_s$ and let us set $w_s = e_s/m_s$. Due to the electroneutrality assumption and for the binary configuration we consider, the ion mass density $\rho_i$ and the electron mass density $\rho_e$ are simply proportional to the total mass density $\rho = \sum_s \rho_s$, *i.e.* $\rho_s = \alpha_s \rho$, and one can check that $\alpha_s = (1 - (w_i/w_e)^{\mathrm{sgn}(e_s)})^{-1}$ (sgn stands for the sign function). The PDEs system that we consider may then write:

$$\begin{aligned}
&\partial_t \rho + \nabla \cdot (\boldsymbol{q}_i + \boldsymbol{q}_e) = 0,\\
&\partial_t \boldsymbol{q}_s + \nabla \cdot (\boldsymbol{q}_s \otimes \boldsymbol{u}_s + p_s I + \Pi_s) = -w_s \alpha_s \rho \nabla U + w_s \boldsymbol{q}_s \times \boldsymbol{B} + \boldsymbol{R}_s,\\
&\nabla \cdot (w_i \boldsymbol{q}_i + w_e \boldsymbol{q}_e) = 0,\\
&\partial_t \varepsilon_s + \nabla \cdot (\varepsilon_s \boldsymbol{u}_s + \boldsymbol{\varphi}_s) = -p_s \nabla \cdot \boldsymbol{u}_s - \Pi_s : \nabla \boldsymbol{u}_s + Q_s\,.
\end{aligned}$$

The terms not yet defined are those for which the Braginskii closure is needed, namely: the collision terms $\boldsymbol{R}_s$ and the viscous stress tensors $\Pi_s$ in the momentum conservation equations, the collision terms $Q_s$ and the heat flux densities $\boldsymbol{\varphi}_s$ in the internal energy equations. These terms are all defined in Section 2.3.

Such a PDEs system shows ten non-linear and coupled scalar PDEs and ten unknown scalar fields. Of course, the equations for the internal energies, $\varepsilon_s$, yield evolution equations for the pressures, $p_s$, by multiplication by $(\gamma - 1)$.

*2.3. Braginskii closures*

The Braginskii closures were proposed in the celebrated paper [9]. Here we simply provide expressions that are not associated to any specific coordinate system, especially the local coordinate system such that one of the axis is aligned on the magnetic field. They are those used in our numerical implementation.

First, it is needed to introduce the cyclotronic angular frequencies $\omega_{cs} = B e_s/m_s$, where $B = |\boldsymbol{B}|$, and the collision times $\tau_s = m_s^{1/2} T_s^{3/2}/(n_s e^4)$. Let us also define $\boldsymbol{u}_\parallel = (\boldsymbol{u}\cdot\boldsymbol{b})\boldsymbol{b}$, with $\boldsymbol{b} = \boldsymbol{B}/B$, for the projection of any vector field $\boldsymbol{u}$ onto the magnetic field lines, and $\boldsymbol{u}_\perp = \boldsymbol{u} - \boldsymbol{u}_\parallel$. Similar notations are used for the gradient operator, *i.e.* $\nabla_\parallel T = (\nabla T \cdot \boldsymbol{b})\boldsymbol{b}$ and $\nabla_\perp T = \nabla T - \nabla_\parallel T$ for any scalar field $T$.

**Collision terms.** The collision terms that appear in the momentum equations compensate. They write $\boldsymbol{R}_e = \boldsymbol{R}$ and $\boldsymbol{R}_i = -\boldsymbol{R}$, with:

$$\begin{aligned}
\boldsymbol{R} &= \boldsymbol{R}_u + \boldsymbol{R}_T,\\
\boldsymbol{R}_u &= -\frac{m_e n_e}{\tau_e}(0.51\boldsymbol{u}_\parallel + \boldsymbol{u}_\perp),\\
\boldsymbol{R}_T &= -0.71 n_e \nabla_\parallel T_e - 1.5\frac{n_e}{\omega_{ce}\tau_e}\boldsymbol{b}\times\nabla T_e,
\end{aligned}$$

where $\boldsymbol{u} = \boldsymbol{u}_e - \boldsymbol{u}_i$.

**Stress tensors.** The stress tensors decompose in three terms:

$$\Pi_s = -\eta_\parallel \Pi_\parallel - \eta_\perp \Pi_\perp + \eta_\wedge \Pi_\wedge,$$

with, omitting the subscript $s$ for the sake of simplicity:

$$\begin{aligned}
\Pi_{\parallel} &= \frac{3}{2}\Big(\boldsymbol{b}\otimes\boldsymbol{b}-\frac{1}{3}I\Big)\Big(\boldsymbol{b}\otimes\boldsymbol{b}:W\Big),\\
\Pi_{\perp} &= \frac{1}{4}\Big(W+3(W\boldsymbol{b}\otimes\boldsymbol{b}+\boldsymbol{b}\otimes\boldsymbol{b}W)+\frac{1}{2}(I-15\boldsymbol{b}\otimes\boldsymbol{b})(\boldsymbol{b}\otimes\boldsymbol{b}:W)\Big),\\
\Pi_{\wedge} &= \frac{1}{4}\Big(M_bW(I+3\boldsymbol{b}\otimes\boldsymbol{b})-(I+3\boldsymbol{b}\otimes\boldsymbol{b})WM_b\Big),
\end{aligned}$$

where $W=\nabla\boldsymbol{u}_s+(\nabla\boldsymbol{u}_s)^t-2/3\nabla\cdot\boldsymbol{u}_sI$ is the strain rate tensor typical of Newtonian fluids and $M_b$ is the antisymmetric matrix such that for any vector $\boldsymbol{u}$, $M_b\boldsymbol{u}=\boldsymbol{b}\times\boldsymbol{u}$. The coefficients write, for the ions:

$$\eta_{\parallel}=0.96n_iT_i\tau_i\,,\quad \eta_{\perp}=1.25\frac{\eta_{\parallel}}{(\omega_{ci}\tau_i)^2}\,,\quad \eta_{\wedge}=1.04\frac{\eta_{\parallel}}{\omega_{ci}\tau_i},$$

and for the electrons :

$$\eta_{\parallel}=0.73n_eT_e\tau_e\,,\quad \eta_{\perp}=2.79\frac{\eta_{\parallel}}{(\omega_{ce}\tau_e)^2}\,,\quad \eta_{\wedge}=-1.37\frac{\eta_{\parallel}}{\omega_{ce}\tau_e}.$$

**Thermal fluxes.** Like the stress tensors, the ion thermal fluxes show three components:

$$\boldsymbol{\varphi}_i=-\kappa^i_{\parallel}\nabla_{\parallel}T_i-\kappa^i_{\perp}\nabla_{\perp}T_i+\kappa^i_{\wedge}\boldsymbol{b}\times\nabla T_i,$$

where :

$$\kappa^i_{\parallel}=3.9\frac{n_iT_i\tau_i}{m_i}\,,\quad \kappa^i_{\perp}=0.51\,\frac{\kappa^i_{\parallel}}{(\omega_{ci}\tau_i)^2}\,,\quad \kappa^i_{\wedge}=0.64\frac{\kappa^i_{\parallel}}{\omega_{ci}\tau_i}.$$

The electron thermal fluxes write, again with $\boldsymbol{u}=\boldsymbol{u}_e-\boldsymbol{u}_i$:

$$\begin{aligned}
\boldsymbol{\varphi}_e &= \boldsymbol{\varphi}^e_u+\boldsymbol{\varphi}^e_T,\\
\boldsymbol{\varphi}^e_u &= n_eT_e(0.71\boldsymbol{u}_{\parallel}+\frac{1.5}{\omega_{ce}\tau_e}\boldsymbol{b}\times\boldsymbol{u}),\\
\boldsymbol{\varphi}^e_T &= -\kappa^e_{\parallel}\nabla_{\parallel}T_e-\kappa^e_{\perp}\nabla_{\perp}T_e+\kappa^e_{\wedge}\boldsymbol{b}\times\nabla T_e,\\
\kappa^e_{\parallel} &= 3.2\frac{n_eeT_e\tau_e}{m_e}\,,\quad \kappa^e_{\perp}=1.47\,\frac{\kappa^e_{\parallel}}{(\omega_{ce}\tau_e)^2}\,,\quad \kappa^e_{\wedge}=0.78\frac{\kappa^i_{\parallel}}{\omega_{ci}\tau_i}.
\end{aligned}$$

*2.4. Expected difficulties*

Let us underline some difficulties associated to the present modeling:

- The PDEs system clearly associates equations that usually correspond to description of compressible flows on the one hand, and to the description of incompressible fluids on the other. This is especially obvious when deriving equations for the total momentum and for the current, see [8]. The governing equations for the momentum are then typical of compressible flows, whereas those for the current are typical of incompressible ones, with the electric potential associated to the divergence free constraint.
- The problem exhibits some multi-scale features. As well known, the particles trajectories show a spiral motion around the magnetic lines, which "Larmor radius" is very small with respect to a characteristic size of the plasma, see *e.g.* [11, 16]. This multi-scale feature in space is associated to a multiscale feature in time, because the "cyclotronic frequency" is much smaller than *e.g.* the discharge time.
- The electrons are about 2000 times lighter than the electrons. In the frame of MHD approaches, this justifies the generalized Ohm law, which is obtained when neglecting the inertial terms in the electron momentum equation.

- The magnetic field is very strong in tokamaks. This leads, in our numerical algorithm, to a strong anisotropic problem on the electrical potential $U$, see Section 3.1.2.
- The Braginskii closures introduce a complex nonlinear coupling between the equations together with strong anisotropy phenomena.
  - The diffusion phenomena are essentially aligned on the magnetic lines, which is mainly associated to the fact that the magnetic field is strong. From the expressions given in Section 2.3, one can observe that

$$\frac{\eta_\perp}{\eta_\parallel} \propto \frac{\kappa_\perp}{\kappa_\parallel} \propto \frac{1}{(\omega_c\tau)^2} \quad , \quad \frac{\eta_\wedge}{\eta_\parallel} \propto \frac{\kappa_\wedge}{\kappa_\parallel} \propto \frac{1}{\omega_c\tau} \, .$$

    Some values, typical of the core and of the edge parts of the plasma, of the anisotropy factor $\omega_c\tau$ are provided in Table 1.

| | Plasma core | Plasma edge |
|---|---|---|
| $T\ (K)$ | $1.16\,10^8$ | $5.8\,10^5$ |
| $n\ (m^{-3})$ | $10^{20}$ | $10^{19}$ |
| $\omega_{ce}\tau_e$ | $3.39\,10^7$ | $1.2\,10^5$ |
| $\omega_{ci}\tau_i$ | $1.12\,10^6$ | $3.96\,10^3$ |

Table 1: Values of the product $\omega_c\tau$ for the ions and the electrons and for temperature-density pairs typical of the core and of the edge of the plasma

  - The parallel transport coefficients may show very high values. Assuming the following reference values (*i.e.* those used in Section 4): $T^\star = 100\,eV$, $n^\star = 10^{19}\,m^{-3}$, $l^\star = 2\,m$, $m^\star = m_{proton}$ and $e^\star = e$, and if we set $u^\star = \sqrt{T^\star/m^\star} = 97861\,ms^{-1}$ and $t^\star = l^\star/u^\star = 2.04\,10^{-5}\,s$, then one may obtain the results shown in Table 2, for both the ions and the electrons and for two different temperature levels typical of the plasma edge. These values may be criticized see e.g. [18], but, in any case, this constitutes an additional difficulty of the physical model.

| | $T$ | $n$ | $f_c$ | $\tau$ | $\eta_\parallel$ | $\kappa_\parallel$ |
|---|---|---|---|---|---|---|
| ions | 0.298 | 0.5 | 291.8 | 2.21 | 0.316 | 1.28 |
| electrons | 0.298 | 0.5 | $5.36\,10^5$ | 0.036 | 0.004 | 31.9 |
| ions | 3.05 | 5.9 | 303 | 6.13 | 106.02 | 430.71 |
| electrons | 3.05 | 5.9 | $5.58\,10^5$ | 0.101 | 1.33 | 10709 |

Table 2: Dimensionless temperature, density, cyclotronic frequency, collision time and parallel transport coefficients for the momentum and energy conservation equations.

## 3. Numerical method

The time discretization is described in Section 3.1 and the formulation of the space discretization is explained in Section 3.2. The anisotropy feature is discussed in Section 3.3. More specific details about the numerical algorithm are given in Section 3.4.

### *3.1. Time scheme*

Due to the strong couplings and non-linearities of the PDEs system, one may prefer an explicit time-scheme rather than an implicit one. However, one may keep attention to the two following points.

- The Lorentz forces should be treated implicitly to avoid numerical instabilities. Indeed, the approximation with an Euler forward scheme of the Ordinary Differential Equation (ODE): $\partial_t \boldsymbol{q} = \boldsymbol{q} \times \boldsymbol{B}$ is unstable, since the exact solution of the ODE is such that:

$$\begin{aligned} \boldsymbol{q} \cdot \partial_t \boldsymbol{q} &= 0\,, \quad |\boldsymbol{q}| = Constant \\ \boldsymbol{b} \cdot \partial_t \boldsymbol{q} &= 0\,, \quad q_{\|} = Constant \end{aligned}$$

  whereas the Euler forward approximation yields: $(\boldsymbol{q}_\perp^{n+1})^2 = (\boldsymbol{q}_\perp^n)^2 + (\delta t |\boldsymbol{B}||\boldsymbol{q}_\perp^n|)^2$ , with $\delta t$ for the time step.

- The divergence free constraint on the current is not an evolution equation and so should be addressed in a different way.

In [8], we suggested to use an implicit-explicit Runge Kutta method (IMEX RK [2]) for the PDEs system of conservation equations, associated to a projection method, at the end of each RK step, for the divergence free constraint. On the basis of the Helmholtz decomposition of any (sufficiently smooth) vector field into gradient and rotational parts, the projection step consisted in, first, computing the electric potential that allows to enforce the divergence free constraint and, then, updating in consequence the ion and electron momentums. However, it has turned out that such a rather natural approach was not satisfactory, yielding time-step dependent results. Some explanations on a simplified model are provided in Appendix B.2. To overcome this difficulty, hereafter we suggest to use a Strang splitting scheme that allows to address the Lorentz force and the divergence free constraint consistently.

*3.1.1. The splitting scheme*

Let us recall that, for the PDE: $\partial_t u + L(u) = 0$, with $L \equiv L_1 + L_2$, the Strang splitting consists in solving, with $n$ for the time index:

$$\begin{aligned} \partial_t u + L_1(u) &= 0\,, t \in (t_n, t_{n+1/2}), \quad u(t_n) \simeq u_n \longrightarrow \tilde{u}^{n+1/2} \simeq u(t_{n+1/2})\,, \\ \partial_t u + L_2(u) &= 0\,, t \in (t_n, t_{n+1}), \quad u(t_n) \simeq \tilde{u}^{n+1/2} \longrightarrow u^{n+1/2} \simeq u(t_{n+1})\,, \\ \partial_t u + L_1(u) &= 0\,, t \in (t_{n+1/2}, t_{n+1}), \quad u(t_{n+1/2}) \simeq u^{n+1/2} \longrightarrow u^{n+1} \simeq u(t_{n+1})\,. \end{aligned}$$

The splitting that we suggest makes use of the structure above. We consider for the System I:

$$\begin{aligned} &\partial_t \rho + \nabla \cdot (\boldsymbol{q}_i + \boldsymbol{q}_e) = 0, \\ &\partial_t \boldsymbol{q}_s + \nabla \cdot (\boldsymbol{q}_s \otimes \boldsymbol{u}_s + p_s I + \Pi_s) = \boldsymbol{R}_s, \\ &\partial_t p_s + \nabla \cdot (p_s \boldsymbol{u}_s + (\gamma - 1)\boldsymbol{\varphi}_s) = (\gamma - 1)(-p_s \nabla \cdot \boldsymbol{u}_s - \Pi_s : \nabla \boldsymbol{u}_s + Q_s), \end{aligned}$$

and we include the Lorentz force and the divergence free constraint in the System II:

$$\begin{aligned} &\partial_t \boldsymbol{q}_s = -w_s \alpha_s \rho \nabla U + w_s \boldsymbol{q}_s \times \boldsymbol{B}, \\ &\nabla \cdot (w_i \boldsymbol{q}_i + w_e \boldsymbol{q}_e) = 0\,. \end{aligned}$$

To integrate each system we suggest to use RK schemes with large absolute stability regions: An explicit RK (ERK) scheme is used for System I, whereas a Diagonally Implicit RK (DIRK) scheme is used for System II. Moreover, because the diffusion terms of System I implies strong stability constraints on the time-step $\delta t$, a sub-time cycling technique is used to integrate the System I with a sub-time-step $\delta t/s$, where $s$ is the number of subcycles. The System II can be recasted to an elliptic problem on the electric potential (see next Section).

The Strang splitting is second order accurate as soon as the schemes used for each step are at least second order accurate, which is the case in our implementation by using RK schemes of order 3. However, it is worth noting that System II will be supplemented with boundary condition to ensure it is well posed. This

inevitably leads to enforce some artificial boundary conditions on the electric potential, probably resulting in some loss of accuracy of the potential approximation. This phenomenon is well known for projection method in incompressible fluid mechanics, which approximates the pressure at an order lower than for the velocity, see *e.g.* [20].

*3.1.2. Resolution of system II. Computation of the potential*

To address the System II, one can first derive an elliptic equation for the potential. At each DIRK step, one has indeed to compute $\boldsymbol{q}_i$, $\boldsymbol{q}_e$ and $U$ such that:

$$\begin{aligned}&\boldsymbol{q}_s = \tilde{\boldsymbol{q}}_s + a\delta t(-w_s\alpha_s\rho\nabla U - w_s B M_b \boldsymbol{q}_s),\\ &\nabla\cdot\sum_s w_s\boldsymbol{q}_s = 0,\end{aligned}$$

where $\tilde{\boldsymbol{q}}_s$ is the previous RK estimate of $\boldsymbol{q}_s$, $a$ the diagonal coefficient (Butcher tableau) of the DIRK scheme, $\delta t$ the time-step and $M_b$ the antisymmetric matrix introduced previously such that $\boldsymbol{b}\times\boldsymbol{q}_s = M_b\boldsymbol{q}_s$. Then, expressing the current and taking its divergence yields:

$$\nabla\cdot A\nabla U = \sum_s w_s\nabla\cdot A_s\tilde{\boldsymbol{q}}_s\,, \tag{2}$$

where $A = \rho\sum_s A_s a\,\delta t\, w_s^2\alpha_s$ and $A_s = (\mathbb{I} + a\,\delta t\, w_s B M_b)^{-1}$. A calculation, postponed to Appendix A, shows that the matrix $A_s$ can be expressed as follows:

$$A_s = (\mathbb{I} - \gamma_s B M_b + \gamma_s^2\boldsymbol{B}\otimes\boldsymbol{B})/(1+\gamma_s^2\boldsymbol{B}^2), \quad \text{with } \gamma_s = a\,\delta t\, w_s. \tag{3}$$

Then, it readily follows from the equality:

$$\big(\boldsymbol{x}, \boldsymbol{x} + \gamma_s\boldsymbol{x}\times\boldsymbol{B} + \gamma_s^2\boldsymbol{B}(\boldsymbol{B}\cdot\boldsymbol{x})\big) = (\boldsymbol{x},\boldsymbol{x}) + \gamma_s^2(\boldsymbol{B}\cdot\boldsymbol{x})^2,$$

that $A_s$ is coercive and, since $a\delta t w_s^2\alpha_s\rho > 0$, $A$ is also coercive.

Thus, $U$ solves a non self adjoint elliptic equation which is well posed, from the Lax-Milgram theorem, in the Sobolev space $H^1$ if Dirichlet conditions are considered or in $H^1/\mathbb{R}$ with admissible Neumann conditions.

Once the potential $U$ is known, one can compute the ion and electron momentums from:

$$\boldsymbol{q}_s = A_s(\tilde{\boldsymbol{q}}_s - a\delta t w_s\alpha_s\rho\nabla U)\,. \tag{4}$$

The following remarks can be expressed:

- The matrices $A_s$ depend on the time-step and on the RK step number, through the coefficient $a$, except if the DIRK scheme is such that its diagonal coefficient (in the Butcher tableau) is constant (this is the case in our implementation).
- The problem (2) exhibits an anisotropy structure, see Section 3.3.
- A natural boundary condition that yields a well posed problem, is obtained by applying the divergence theorem to both sides of (2) and stating that the equality is verified everywhere on the boundary

$$(A\nabla U - \sum_s w_s A_s\tilde{\boldsymbol{q}}_s)\cdot\boldsymbol{n} = 0, \tag{5}$$

  where $\boldsymbol{n}$ is the unit outwards vector normal to the boundary $\Gamma$ of the computational domain. By summing the equation (4), expressed for the ions and the electrons and weighted by the coefficients $w_s$, one easily checks that the boundary condition (5) is equivalent to the condition $\boldsymbol{j}\cdot\boldsymbol{n} = 0$, *i.e.* an impermeability condition for the end-of-step current, which of course is consistent with the divergence free constraint.

*3.2. Fourier-SEM spatial approximation*

The tokamak is represented in cylindrical coordinates $(r, z, \theta)$ by the periodic domain $\Omega = \hat{\Omega} \times [0, 2\pi]$. The Fourier-SEM method consists of using a Fourier approximation in the toroidal direction $\theta$ and the SEM in the poloidal plane $\hat{\Omega}$. Hence, let us introduce an integer $K_\theta$ which stands for the number of grid points (or $rz$-planes) used for the discretization in the toroidal direction, an unstructured quadrangular mesh of the poloidal plane $\hat{\Omega}$ and an integer $N$ which stands for the polynomial approximation degree in each element. We denote by $\varphi_m(r, z)$ the SEM basis function associated to the grid point of index $m$ in $\hat{\Omega}$. Recall that, on the reference element, SEM basis functions are obtained by tensorial product of the Lagrange polynomials (of degree $N$) based on the $N + 1$ Gauss-Lobatto-Legendre 1D nodes.

For the sake of simplicity we first focus on the toy PDE:

$$\partial_t u + \nabla \cdot \boldsymbol{f} = s,$$

where $\boldsymbol{f}$ is typically a diffusion flux term, to which an integration by parts is to be applied. The advection flux term is assumed included in the source term $s$. The weak formulation of this PDE writes:

$$\int_\Omega v \partial_t u \, d\Omega + \int_\Gamma v \boldsymbol{f} \cdot d\Gamma - \int_\Omega \boldsymbol{f} \cdot \nabla v \, d\Omega = \int_\Omega v s \, d\Omega.$$

In the Fourier space, $u \simeq \sum_k \hat{u}_k(r, z) e^{\mathrm{i}k\theta}$, with $|k| \leq K_\theta/2$ and $\mathrm{i}^2 = -1$. The $\hat{u}_k$ and $\hat{u}_{-k}$ are complex conjugate since $u$ is a real function. It is natural to use, in each spectral element, basis functions of the form $\varphi_m(r, z)e^{\mathrm{i}l\theta}$. Then, since (i) in the cylindrical coordinate system $d\Omega = r d\theta d\hat{\Omega}$ and (ii) the $L^2$ hermitian product, in $\theta \in (0, 2\pi)$, of $e^{\mathrm{i}k\theta}$ and $e^{\mathrm{i}l\theta}$ equals $2\pi\delta_{k-l,0}$ ($\delta$, Kronecker symbol), one obtains the expression that should hold for any Fourier mode $k$ and any SEM basis function $\varphi_m(r, z)$:

$$\int_{\hat{\Omega}} r \, \varphi_m \, \partial_t \hat{u}_k \, d\hat{\Omega} + \int_{\hat{\Gamma}} r \, \varphi_m \, \hat{\boldsymbol{f}}_k \cdot d\hat{\Gamma} - \int_{\hat{\Omega}} r \, \hat{\boldsymbol{f}}_k \cdot \hat{\nabla} \varphi_m \, d\hat{\Omega} = \int_{\hat{\Omega}} r \, \varphi_m \, \hat{s}_k \, d\hat{\Omega} \,,$$

where, if using the usual dot product: $\hat{\nabla}\varphi_m = (\ \partial_r \varphi_m,\ -\mathrm{i}k\varphi_m/r,\ \partial_z \varphi_m\ )$.

Things are slightly more complicated in the vectorial case

$$\partial_t \boldsymbol{u} + \nabla \cdot f = \boldsymbol{s},$$

where $f$ is now a second order tensor. After multiplication by the vector test function $\boldsymbol{v}$ and integration by parts, one finds:

$$\int_\Omega \boldsymbol{v} \cdot \partial_t \boldsymbol{u} \, d\Omega + \int_\Gamma \boldsymbol{v} \cdot f \, d\Gamma - \int_\Omega f : \nabla \boldsymbol{v} \, d\Omega = \int_\Omega \boldsymbol{v} \cdot \boldsymbol{s} \, d\Omega.$$

Taking into account the cross terms in the divergence operator, when expressed in the cylindrical coordinate system, and specializing the components of $\boldsymbol{v}$ to the $r$, $\theta$ and $z$ components of the PDE one obtains:

$$\begin{aligned}
\int_\Omega v_r \partial_t u_r \, d\Omega + \int_\Gamma v_r (f d\Gamma)_r &= \int_\Omega (\boldsymbol{f}_{r.} \cdot \nabla v_r + f_{\theta\theta} v_r / r) \, d\Omega + \int_\Omega v_r s_r \, d\Omega, \\
\int_\Omega v_\theta \partial_t u_\theta \, d\Omega + \int_\Gamma v_\theta (f d\Gamma)_\theta &= \int_\Omega (\boldsymbol{f}_{\theta.} \cdot \nabla v_\theta - f_{r\theta} v_\theta / r) \, d\Omega + \int_\Omega v_\theta s_\theta \, d\Omega, \\
\int_\Omega v_z \partial_t u_z \, d\Omega + \int_\Gamma v_z (f d\Gamma)_z &= \int_\Omega \boldsymbol{f}_{z.} \cdot \nabla v_z \, d\Omega + \int_\Omega v_z s_z \, d\Omega,
\end{aligned}$$

where for example, $\boldsymbol{f}_{r.} = (f_{rr}, f_{r\theta}, f_{rz})$. The corresponding expressions in Fourier space follow easily.

Finally, one should address the elliptic potential equation (2), that may write, with obvious notation:

$$\nabla \cdot A \nabla U = \nabla \cdot \boldsymbol{s}.$$

In weak form and assuming the natural boundary condition (5), one obtains:

$$\int_\Omega A\nabla U\cdot\nabla v=\int_\Omega \boldsymbol{s}\cdot\nabla v\,.$$

One notices that tensor $A$ only depends on $\theta$ via the density $\rho$. Let us assume, in a first step, that $\rho(r,z,\theta)\approx\hat{\rho}_0(r,z)$, then one obtains for each Fourier mode $k$:

$$\int_{\hat\Omega} rA\hat{\nabla}\hat{U}_k\cdot\hat{\nabla}\varphi_m\,d\hat{\Omega}=\int_{\hat\Omega} r\hat{\boldsymbol{s}}_k\cdot\hat{\nabla}\varphi_m\,d\hat{\Omega}.$$

Thus, we have substituted a set of 2D like problems to the initial 3D one. The methodology is then standard, setting up a stiffness matrix, the right hand side and then solving. However, on the contrary of what will be obtained for a Poisson equation, it should be noticed that the real and imaginary parts of each mode are coupled by the non-diagonal terms of the tensor $A$.

The space variations of $\rho$ mainly occur in the poloidal plane, so that one only expects small fluctuations in the toroidal direction. To take them into account one may think to use a fixed point procedure, but this remains to be included in our numerical implementation.

*3.3. Anisotropic diffusion*

As already mentioned, the Braginskii closures yield strongly anisotropic problems. When using a mesh non-aligned on the magnetic field, difficulties are then generally observed [13, 14]. Typically, one should handle expressions of the form:

$$\boldsymbol{\varphi}=-\kappa_\parallel\nabla_\parallel T-\kappa_\perp\nabla_\perp T+\kappa_\wedge(\boldsymbol{b}\times\nabla T)\,.$$

To this end, we introduce a diffusion tensor such that, see [8] for details:

$$\boldsymbol{\varphi}=-K\nabla T\,,\quad K=(\kappa_\parallel-\kappa_\perp)\,\boldsymbol{b}\otimes\boldsymbol{b}+\kappa_\perp\,\mathbb{I}+\kappa_\wedge M_b$$

that can be easily handled thanks to the weak formulation on which relies the SEM.

For the sake of completeness, let us mention that [8]:

- The $\nabla\cdot\kappa_\wedge(\boldsymbol{b}\times\nabla T)$ term behaves like a transport term with velocity

  $$\boldsymbol{u}_\wedge=\nabla\kappa_\wedge\times\boldsymbol{b}+\kappa_\wedge\nabla\times\boldsymbol{b}$$

  It is thus associated to curvature effects or to the inhomogeneity of the temperature dependent $\kappa_\wedge$ coefficient.

- Using the Fourier-SEM approach, satisfactory numerical results have been obtained. Especially, we have considered an unsteady diffusion problem in a torus with magnetic lines not aligned on a mesh and have obtained very satisfactory results for the extreme case $\kappa_\perp/\kappa_\parallel=0$. Moreover, comparisons carried out with $P_1$ finite elements have outlined the importance of using a high order method, if not using a mesh aligned on the magnetic lines [7].

At this point, it is of interest to point out that independently of the Braginskii closures, the elliptic PDE that the potential solves, see (2), also shows a strong anisotropy. Indeed, the diffuse flux $A\nabla U$ can be recasted as follows:

$$A\nabla U=A_\parallel\nabla_\parallel U+A_\perp\nabla_\perp U+A_\wedge(\boldsymbol{b}\times\nabla U),$$

with

$$A_\parallel=\rho a\,\delta t\,\sum_s w_s^2\alpha_s,\quad A_\perp=\rho a\,\delta t\,\sum_s\frac{w_s^2\alpha_s}{1+\gamma_s^2\boldsymbol{B}^2},\quad A_\wedge=\rho a\,\delta t\,\sum_s\gamma_s\frac{w_s^2\alpha_s}{1+\gamma_s^2\boldsymbol{B}^2}\gamma_s.$$

This points at the anisotropy ratio:

$$\frac{A_\perp}{A_\parallel} = \frac{\sum_s \dfrac{w_s^2 \alpha_s}{1+\gamma_s^2 \boldsymbol{B}^2}}{\sum_s w_s^2 \alpha_s}.$$

Clearly, this ratio depends on the time-step through the coefficients $\gamma_s$. In the limit $\delta t = 0$, one has $A_\perp/A_\parallel = 1$. More interesting, one can estimate this ratio for the following extreme values of the time-step: $\delta t = 2\pi/\omega_{ci}$ and $\delta t = 2\pi/\omega_{ce}$, that are associated to the ion and electron cyclotronic angular frequencies. We find, in the first case $A_\perp/A_\parallel \approx 5.01\ 10^{-5}$ and in the second case $A_\perp/A_\parallel \approx 9.24\ 10^{-2}$. Hence, for the values of the time step used in the simulations, the potential solves a strongly anisotropic elliptic PDE.

*3.4. Computational details*

- In order to evaluate in the most accurate way the advective and diffusive fluxes, it is *a priori* preferable to formulate them in terms of the computational variables, *i.e.* the density and the ion and electron momentum and pressures. Thus, from $p_s = \rho_s T_s$ and $\boldsymbol{q}_s = \rho_s \boldsymbol{u}_s$, one obtains for the temperature and velocity gradients:

$$\begin{aligned} \partial_j T_s &= T_s\left(\frac{\partial_j p_s}{p_s} - \frac{\partial_j \rho}{\rho}\right), \\ \partial_j u_i^s &= \frac{1}{\rho}(\partial_j q_i^s/\alpha_s - u_i^s \partial_j \rho). \end{aligned}$$

  Let us recall that in the cylindrical coordinate system the velocity gradient tensor shows cross terms:

$$\nabla \boldsymbol{u}^s = \begin{pmatrix} \partial_r u_r^s & \frac{1}{r}(\partial_\theta u_r^s - u_\theta^s) & \partial_z u_r^s \\ \partial_r u_\theta^s & \frac{1}{r}(\partial_\theta u_\theta^s + u_r^s) & \partial_z u_\theta^s \\ \partial_r u_z^s & \frac{1}{r}\partial_\theta u_z^s & \partial_z u_z^s \end{pmatrix},$$

  and that the divergence of the velocity equals its trace.

  Concerning the advective fluxes one uses:

$$\begin{aligned} \nabla \cdot p_s \boldsymbol{u}_s &= \boldsymbol{u}_s \cdot \nabla p_s + p_s \nabla \cdot \boldsymbol{u}_s, \\ \nabla \cdot (\boldsymbol{q}_s \otimes \boldsymbol{u}_s + p_s I) &= \nabla \boldsymbol{q}_s\, \boldsymbol{u}_s + \nabla \cdot \boldsymbol{u}_s\, \boldsymbol{q}_s + \nabla p_s. \end{aligned}$$

- To solve the algebraic system associated to the potential, we use a static condensation technique: The unknowns associated to the inner grid-points of each element are eliminated, so that one only solves for the unknowns located on the edges of the elements. The algorithm is the one described in [26]. The system is then of smaller dimension, *i.e.* $O(N)$ rather than $O(N^2)$ ($N$, polynomial approximation degree) and better conditioned, *i.e.* $O(N)$ rather than $O(N^3)$ [30].

- A BICGSTAB algorithm is used to solve this non-symmetric algebraic system for the potential. In a matrix free implementation of the method, we are limited to the use of a Jacobi preconditioner. When assembling the stiffness matrix (in sparse manner), the best results have been obtained with the algebraic multigrid preconditioner HYPRE used through the PETSc software. It requires only few iterations of the BICGSTAB algorithm (about ten).

- In the explicit part, a spectral vanishing viscosity (SVV) technique is used for stabilization, see *e.g.* [37]. This allows to address stiff problems together with preserving the "spectral accuracy" of the Fourier-SEM approximation.

- Isoparametric mappings may be used to take into account the curvature, in the poloidal plane, of the boundary of the computational domain. The technique is based on a bending procedure similar to the one proposed in [26] for triangular elements.

## 4. Preliminary investigations

We consider the JET tokamak which is located at Culham, UK, and operated by the Culham Centre for Fusion Energy. In Section 4.1, we describe precisely the physical problem we solve, that is the geometry of the domain and of the magnetic field, the reference values used to get a dimensionless model, and the initial and boundary conditions. Some numerical results are given in Section 4.2.

### *4.1. The physical problem*

#### *4.1.1. Geometry and magnetic field*

The geometry of the edge part of the plasma, in the poloidal plane, together with a mesh aligned on the magnetic surfaces, was provided to us in the frame of collaborations with partners working on the MHD JOREK code [15]. Fig. 1 shows the computational domain and the mesh, which is composed of quadrangular elements. Using such a mesh, it is possible to implement the SEM using any polynomial approximation degree $N > 1$ in each element.

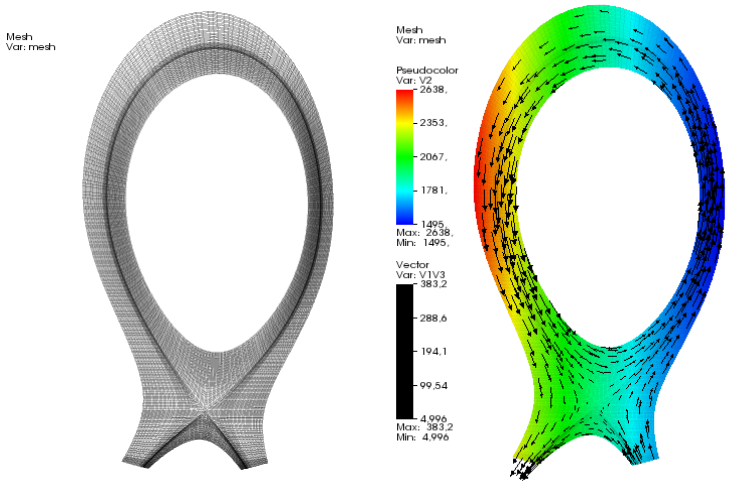


Figure 1: Computational domain and mesh (at left); Visualization of the magnetic field (at right).

The magnetic field is also shown in Fig. 1. It is obtained with the JOREK software when solving the Grad-Shafranov equilibrium $\nabla p = \boldsymbol{j} \times \boldsymbol{B}$. Such a computation provides the density $\rho$, the (total) pressure $p$, and the magnetic potential $\psi$. For the poloidal component $\boldsymbol{B}_p$, one defines

$$\boldsymbol{B}_p = \frac{1}{r}\Big( -\partial_z\psi,\ 0,\ \partial_r\psi \Big),$$

and one assumes, for the toroidal component: $B_\theta = C/r$ ($r$: dimensionless distance at the axis of the tokamak, $C$: a constant equal to 3 in our simulations).

#### *4.1.2. Nondimensionalization*

Dimensionless values are hereafter systematically used. The values of reference quantities are chosen as follows:

mass: $m^\star \equiv m_i = 1.673\,10^{-27}\,kg$ (proton mass), electric charge: $e^\star \equiv -e_e = 1.6022\,10^{-19}\,C$,
length: $l^\star = 2\,m$, temperature: $T^\star = 100\,eV$,
particles density: $n^\star = 10^{19}\,m^{-3}$.

The other reference quantities are coherently defined:

| | |
|---|---|
| density: $\rho^\star = n^\star m^\star$, | velocity: $u^\star = \sqrt{e^\star T^\star / m^\star}$, |
| time: $t^\star = l^\star / u^\star$, | current density: $j^\star = n^\star e^\star u^\star$, |
| magnetic field: $B^\star = m^\star u^\star / (e^\star l^\star)$, | electric potential: $U^\star = m^\star u^{\star 2}$, |
| pressure, energy, viscous tensor: $p^\star = \rho^\star u^{\star 2}$, | heat flux density: $\varphi^\star = \rho^\star u^{\star 3}$. |

*4.1.3. Boundary conditions*

At the internal surface of the computational domain, *i.e.* against the plasma core, we assume Dirichlet conditions for all variables, except the potential. They will be supposed constant in time and so defined by the initial conditions. Elsewhere, no boundary conditions are enforced for the density since the fluid is supposed to be only outgoing.

At the outer surface, excluding the plates, we assume free-slip like conditions for the ion and electron momentums. Thus, in the explicit part of the algorithm (system I, see Section 3), we enforce these vector fields to be tangent to the boundary. At this part of the outer surface, natural boundary conditions, *i.e.* homogeneous Neumann conditions, are used for the pressures.

At the plates, *i.e.* at the remaining parts of the outer surface where the magnetic lines impact the boundary, we use the so-called Bohm boundary conditions. In their simplest form, this means that one should have $M_\parallel \geq 1$, where $M_\parallel$ is the ion parallel Mach number. More elaborate conditions are *e.g.* provided in [27, 35]. On the basis of investigations carried out on a one-dimensional "minimal transport model" [22], we control the ion velocity by varying the density and preserve the ion and electron momentums [31]. Moreover, in this simplified frame we also assume that the temperatures are preserved, so that the pressures vary like the density. Thus, with ($c$, sound velocity):

$$M_\parallel^2 = \frac{(\boldsymbol{u}_i \cdot \boldsymbol{b})^2}{c^2} = \frac{(\boldsymbol{q}_i \cdot \boldsymbol{b})^2}{\gamma \alpha_i \rho^2 \sum_s \alpha_s T_s / m_s} \,,$$

the algorithm is the following: If $M_\parallel < 1$, then set $\rho := \rho / M_\parallel$ and $p_s := p_s / M_\parallel$.

*4.1.4. Initial conditions*

To set up the initial conditions, we again start from a Grad-Shafranov equilibrium obtained with the Jorek software. The difficulty comes from the fact that one has to go from single fluid (axisymmetric) results, say the density $\rho$ and the total pressure $p$, to two-fluid ones. Taking into account the electroneutrality assumption $\sum_s n_s e_s = 0$ yields: $\rho = \sum_s n_s m_s = n_i (m_i - m_e e_i / e_e)$ and thus the value of $n_i$. Then, knowing the total pressure $p = \sum_s p_s$ and assuming equal the ion and electron "temperatures", $T_i$ and $T_e$, one obtains $p = \sum_s n_s T_s = n_i T_i (1 - e_i / e_e)$, which yields the value of $T_i (= T_e)$. Visualizations of the density and of the temperature at the initial time are given in Fig. 2.

To compute the momentums at $t = 0$, one first defines the current. When taking into account the axisymmetry of the magnetic field $\boldsymbol{B}$ and the assumption $B_\theta = C/r$, from the Ampère theorem one finds that the current $\boldsymbol{j}$ is azimuthal:

$$\boldsymbol{j} \propto \nabla \times \boldsymbol{B} = (\partial_z B_r - \partial_r B_z) \boldsymbol{e}_\theta \,,$$

so that $\nabla \cdot \boldsymbol{j} = 0$, *i.e.* $\boldsymbol{j}$ is identically divergence free, and $\boldsymbol{j} \cdot \nabla p = 0$, as desired. Then, we compute $\boldsymbol{j}(t = 0)$, in such a way that the Grad-Shafranov equilibrium relation $\nabla p = \boldsymbol{j} \times \boldsymbol{B}$ is at best verified. From the minimization, at each grid-point, of the Euclidean norm of the residual one obtains:

$$j_\theta = \frac{1}{\boldsymbol{B}_p^2} (B_z \partial_r p - B_r \partial_z p) \,.$$

Then, we define the ion velocity, assuming : (i) $\boldsymbol{u}_i = 0$ inside the separatrix and (ii) $\boldsymbol{u}_i$ colinear to the magnetic field in the SOL: $\boldsymbol{u}_i = u_\parallel \boldsymbol{b}$. The parallel velocity $u_\parallel$ is defined by enforcing $M_\parallel = \pm 1$ at the plates, and by assuming linear variations along the magnetic lines. One can then compute the ion momentum $\boldsymbol{q}_i$.

The electron momentum $\boldsymbol{q}_e$ is finally computed from the expression $\boldsymbol{j} = \sum_s w_s \boldsymbol{q}_s$.

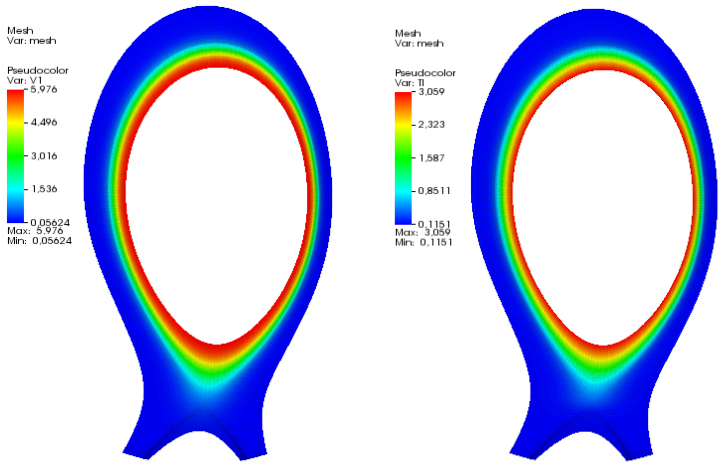


Figure 2: Density $\rho$ (at left) and temperature $T_i = T_e$ (at right), at $t = 0$.

*4.2. Numerical results*

To point out the influence of the Braginskii modeling, we compare results obtained in the Euler approximation (simulation S0) to results obtained using the Braginskii closures (simulations S1 and S2). To make easier the computation, (i) as *e.g.* in [34] we use the heavy electron approximation $m_i/m_e = 100$, and (ii) the parallel transport coefficients of the ion and of the electron have been divided by 100 and by 500, respectively, in simulation S1, and by 10 and 50, in simulation S2.

Using the sequential version of the code, calculations have been done in an axisymmetric configuration, using 3417 spectral elements with polynomial approximation in each variable of degree $N = 3$. Then, the number of grid-points equals 31194 and one has 10 unknowns per grid-point. The dimensionless time-step is taken equal to $\delta t = 5\,10^{-6}$ (reference time: $2.044\,10^{-5}\,s$). The S0 and S1 computations have been done with 5 subcycles, see details in Section 3.1.1, whereas 50 subcycles have been used for the simulation S2. It should be noticed that present space discretization is probably not sufficient. Indeed, the dimensionless ion Larmor radius is $O(1/B)$, with $B \equiv |\boldsymbol{B}| = O(10^3)$ and the dimensionless surface of the computational domain equals $S = 0.7816$. Then, $SB^2 = O(10^6) \gg 31194$ grid-points are required to go at the scale of the ion Larmor radius. This is why the following results should be considered as preliminary ones.

Visualizations of the ion velocity and of the current at $t = 0.02$ are provided for the Euler computation in Fig. 3. As expected, ions are outgoing at the plates and the current is essentially confined inside the separatrix. On animations of these fields, one clearly observes high frequency oscillations of the poloidal component. Qualitatively, differences between the Euler and Braginskii computations are weak: when using the Braginskii closures, the vector fields are better aligned on the magnetic field and the oscillations are of weaker amplitude, especially for simulation S2. In all simulations, the density and pressures evolve weakly, so that the visualizations look like those in Fig. 2. More attentively, the main variations are observed in the immediate vicinity of the plates, where the Bohm conditions apply.

Visualizations of the potential at time $t = 0.02$ are provided for the simulations S0 and S1 in Fig. 4. One can observe the stabilizing effect of the Braginskii closures, with space variations of weaker amplitude for the Braginskii computation. On animations one clearly observes a rotation motion of the potential extrema.

More quantitative results are provided in Fig. 5, which shows the evolution at the point $(r = 1.25, z = 0.056)$ of the $z$-component of the ion momentum. Again, the stabilizing effect of the Braginskii closures is visible, and clearly more important when increasing the values of the parallel transport coefficients, *i.e.* more important for simulation S2 than for S1. From these curves, especially from the zoom in Fig. 5 (right),

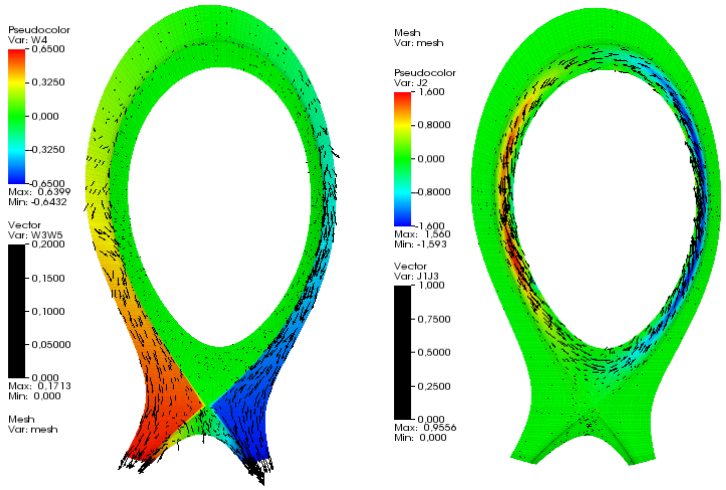


Figure 3: Ion velocity (at left) and current density (at right) for the Euler computation, at $t = 0.02$. Colors are associated to the azimuthal component and arrows to the poloidal one.

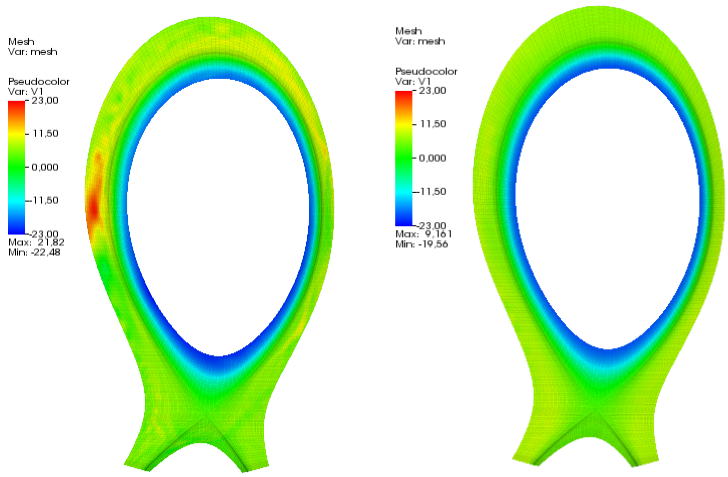


Figure 4: Potential for the Euler (at left) and Braginskii S1 (at right) computations at $t = 0.02$.

one can discern that the oscillations in the poloidal plane are characterized by two dominant frequencies: $f_1 \approx 40$ and $f_2 \approx 3000$. At the considered point, one has $B = 2375$, so that the dimensionless ion cyclotronic frequency equals $f_{ic} = Be/(2\pi m_i) = B/(2\pi) \approx 378$. Taking in mind that in the present computations $m_i = 100\, m_e$, the dimensionless electron cyclotronic frequency equals $f_{ec} = 100 f_{ic} = 37800$.

At this point, it is of interest to compare such frequencies with the one obtained for the toy model considered in Appendix B.1. Clearly, the toy model frequency $f = B/(2\pi\sqrt{m_e/m_i}) = 3780$ is close to the high frequency $f_2 \approx 3000$ obtained in the simulations (at the considered point). Hence, from both the present simulations and the simplified theoretical analysis, it turns out to be useless to capture the very high frequency associated to the electron cyclotronic motion. The maximum value of the magnetic field $\max B \approx 2655$ can be associated to the maximum frequency $f \approx 4226$. Thus, contrarily to the space discretization, the time step $\delta t = 5\, 10^{-6}$ used in the computations was certainly small enough. For the true

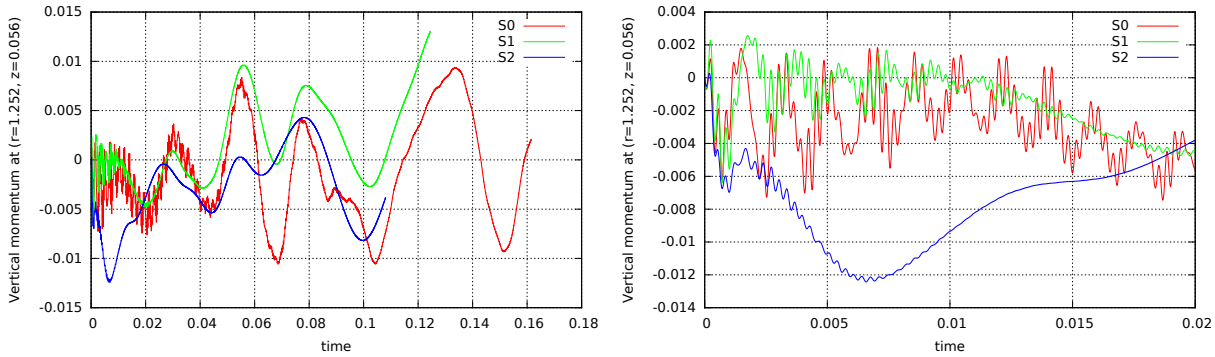


Figure 5: Time-variation of the $z$-component of the ion momentum for the Euler and for the two Braginskii computations (at left) and zoom for $t \in (0, 0.02)$ (at right).

ratio $m_i/m_e \approx 1836$, one can expect that it is enough to capture a frequency $f = \sqrt{m_i/m_e} f_{ic} \approx 42.8 \max f_{ic}$.

## 5. Conclusion

A Fourier-SEM solver has been developed to solve the full Braginskii system in complex geometries, and preliminary results have been presented for the JET tokamak configuration. A parallel version of the code, that makes use of a domain decomposition both in the poloidal plane and in the azimuthal direction, is already operational. This will allow, in next future, to carry out more relevant simulations. Some difficulties however remain: especially, we have used the heavy electron approximation and the parallel transport coefficients have been lowered; Also, one may think that more involved Bohm conditions are required (temperature dependent, more stable at the plates ends) to obtain fully reliable results.

## Appendix A. Proof of (3)

We aimed at deriving an explicit expression of $A_s = (\mathbb{I} + a\,\delta t\, w_s B M_b)^{-1}$. Let us set $\gamma_s = a\,\delta t\, w_s$ and consider $\boldsymbol{u} = A_s \boldsymbol{v}$ then we have:

$$\boldsymbol{v} = \boldsymbol{u} - \gamma_s \boldsymbol{u} \times \boldsymbol{B} \quad \text{and} \quad \boldsymbol{u} = \boldsymbol{v} + \gamma_s \boldsymbol{u} \times \boldsymbol{B}\,.$$

Hence, from the last equality we can deduce that:

$$\boldsymbol{u} \cdot \boldsymbol{B} = \boldsymbol{v} \cdot \boldsymbol{B}\,, \quad \boldsymbol{u} \times \boldsymbol{B} = \boldsymbol{v} \times \boldsymbol{B} - \gamma_s \boldsymbol{B} \times (\boldsymbol{u} \times \boldsymbol{B}).$$

Bearing in mind that $\boldsymbol{B} \times (\boldsymbol{u} \times \boldsymbol{B}) \equiv \boldsymbol{u}(\boldsymbol{B} \cdot \boldsymbol{B}) - \boldsymbol{B}(\boldsymbol{B} \cdot \boldsymbol{u})$, we find:

$$\boldsymbol{u} \times \boldsymbol{B} = \boldsymbol{v} \times \boldsymbol{B} - \gamma_s \boldsymbol{B}^2 \boldsymbol{u} + \gamma_s \boldsymbol{B}(\boldsymbol{B} \cdot \boldsymbol{v}),$$

so that we have:

$$(1 + \gamma_s^2 \boldsymbol{B}^2)\boldsymbol{u} = \boldsymbol{v} + \gamma_s \boldsymbol{v} \times \boldsymbol{B} + \gamma_s^2 \boldsymbol{B}(\boldsymbol{B} \cdot \boldsymbol{v}) = (\mathbb{I} - \gamma_s B M_b + \gamma_s^2 \boldsymbol{B} \otimes \boldsymbol{B})\boldsymbol{v}.$$

This prove (3).

## Appendix B. Study of a simplified model

We address in this section the following toy model:

$$\begin{cases} \rho \equiv \text{constant}, \\ \partial_t \boldsymbol{q}_s = -w_s \alpha_s \rho \nabla U + w_s \boldsymbol{q}_s \times \boldsymbol{B}, \qquad s \in \{i, e\}, \\ \nabla \cdot (w_i \boldsymbol{q}_i + w_e \boldsymbol{q}_e) = 0. \end{cases}$$

We aimed at (i) learning some information about the influence of the divergence-free constraint $\nabla \cdot (w_i \boldsymbol{q}_i + w_e \boldsymbol{q}_e) = 0$ on the behavior of $\boldsymbol{q}_i$ and $\boldsymbol{q}_e$ (see Section Appendix B.1), (ii) understanding how the solution of this toy model can be approximated by a projection method (see Section Appendix B.2).

Let us assume that $e_i = -e_e$ and introduce the ratio $\varepsilon = m_e/m_i$. The (dimensionless) values of the coefficients $w_s$ and $\alpha_s$ can be expressed in terms of $\varepsilon$: $w_i = 1$, $w_e = -1/\varepsilon$, $\alpha_i = 1/(1+\varepsilon)$, $\alpha_e = \varepsilon/(1+\varepsilon)$, and the above system can be recasted using the total momentum $\boldsymbol{q} = \boldsymbol{q}_i + \boldsymbol{q}_e$, the current $\boldsymbol{j} = w_i \boldsymbol{q}_i + w_e \boldsymbol{q}_e$ and $\Psi = \rho U$:

$$\begin{cases} \partial_t \boldsymbol{q} = \boldsymbol{j} \times \boldsymbol{B}, \\ \varepsilon \partial_t \boldsymbol{j} + \nabla \Psi = \Big( \boldsymbol{q} - (1-\varepsilon) \boldsymbol{j} \Big) \times \boldsymbol{B}, \\ \nabla \cdot \boldsymbol{j} = 0. \end{cases} \tag{B.1}$$

To make the calculation easy, we assume that the problem is solved in a smooth bounded 2D domain $\Omega$ embedded in the $(x, y)$-plane, that $\boldsymbol{B} = B \boldsymbol{e}_z$ is uniform and aligned with the $z$-axis and that the total momentum $\boldsymbol{q}_0$ and the current $\boldsymbol{j}_0$ at initial time satisfy $\boldsymbol{q}_0, \boldsymbol{j}_0 \in \text{span}\{\boldsymbol{e}_x, \boldsymbol{e}_y\}$, where $(\boldsymbol{e}_x, \boldsymbol{e}_y, \boldsymbol{e}_z)$ stands for the canonical basis of $\mathbb{R}^3$. The system ensures that $\boldsymbol{q}, \boldsymbol{j} \in \text{span}\{\boldsymbol{e}_x, \boldsymbol{e}_y\}$ for all time. Note also that, in this simplified (2D) geometry, we have, for any field $\boldsymbol{u}$:

$$\nabla \cdot \big( \boldsymbol{u} \times \boldsymbol{B} \big) = B \, \nabla \times \boldsymbol{u}, \quad \nabla \times \big( \boldsymbol{u} \times \boldsymbol{B} \big) = -B \, \nabla \cdot \boldsymbol{u}, \quad \text{and} \quad \big( \boldsymbol{u} \times \boldsymbol{B} \big) \cdot \boldsymbol{\tau} = -B \, \boldsymbol{u} \cdot \boldsymbol{n}, \tag{B.2}$$

where the vectors colinear to $\boldsymbol{e}_z$ are assimilated to scalar quantities, the vector $\boldsymbol{n} = (n_x, n_y)$ stands for the (unit) outward normal vector at the boundary of the domain $\Omega$, and $\boldsymbol{\tau} = (-n_y, n_x)$ is a tangent vector at the boundary of $\Omega$.

Finally, the system is supplemented with the boundary condition $\boldsymbol{j} \cdot \boldsymbol{n} = 0$ on the whole boundary.

### *Appendix B.1. Exact solutions of model* (B.1)

The first observation is that the boundary condition imposed on $\boldsymbol{j}$ implies a boundary condition for $\boldsymbol{q}$. Indeed, from the first equation of (B.1) and the last equality of (B.2) we obtain:

$$\partial_t \big( \boldsymbol{q} \cdot \boldsymbol{\tau} \big) = -B \, \boldsymbol{j} \cdot \boldsymbol{n} = 0, \quad \text{on the boundary.}$$

It means that the boundary condition $\boldsymbol{q} \cdot \boldsymbol{\tau} = \boldsymbol{q}_0 \cdot \boldsymbol{\tau}$ ($\boldsymbol{q}_0$ for the initial state) is implicitly enforced.

Due to these boundary conditions, the vectors $\boldsymbol{j}$ and $\boldsymbol{q}$ are entirely determined by their divergence and rotational (considered as a scalar). Let us denote $\mathrm{d}_{\boldsymbol{j}} = \nabla \cdot \boldsymbol{j}$, $\mathrm{r}_{\boldsymbol{j}} = \nabla \times \boldsymbol{j}$, $\mathrm{d}_{\boldsymbol{q}} = \nabla \cdot \boldsymbol{q}$ and $\mathrm{r}_{\boldsymbol{q}} = \nabla \times \boldsymbol{q}$. By taking the divergence and the rotational of the two first equations of system (B.1) and bearing in mind that $\nabla \cdot \boldsymbol{j} = 0$, we find:

$$\partial_t \mathrm{d}_{\boldsymbol{q}} = B \, \mathrm{r}_{\boldsymbol{j}}, \tag{B.3}$$

$$\partial_t \mathrm{r}_{\boldsymbol{q}} = 0, \tag{B.4}$$

$$\varepsilon \, \partial_t \mathrm{r}_{\boldsymbol{j}} = -B \, \mathrm{d}_{\boldsymbol{q}}, \tag{B.5}$$

$$\mathrm{d}_{\boldsymbol{j}} = 0. \tag{B.6}$$

Thus, the system of PDEs (B.1) is replaced by a set of systems of ODEs (a system for each point of $\Omega$). Each of them can be readily solved. Combining the time derivative of (B.5) and the equation (B.3), we obtain:

$$\partial_{tt} \mathrm{r}_{\boldsymbol{j}} = -\frac{B^2}{\varepsilon}\, \mathrm{r}_{\boldsymbol{j}}.$$

This allows to find the exact expressions of $\mathrm{r}_{\boldsymbol{j}}$ and $\mathrm{d}_{\boldsymbol{q}}$:

$$\mathrm{r}_{\boldsymbol{j}} = \mathrm{r}_{\boldsymbol{j}_0} \cos\Big(\frac{B}{\sqrt{\varepsilon}}t\Big) - \frac{1}{\sqrt{\varepsilon}}\mathrm{d}_{\boldsymbol{q}_0} \sin\Big(\frac{B}{\sqrt{\varepsilon}}t\Big),$$

$$\mathrm{d}_{\boldsymbol{q}} = \sqrt{\varepsilon}\mathrm{r}_{\boldsymbol{j}_0} \sin\Big(\frac{B}{\sqrt{\varepsilon}}t\Big) + \mathrm{d}_{\boldsymbol{q}_0} \cos\Big(\frac{B}{\sqrt{\varepsilon}}t\Big).$$

Finally, from their divergence and rotational we can go back to $\boldsymbol{j}$ and $\boldsymbol{q}$:

$$\boldsymbol{j} = \boldsymbol{j}_0 \cos\Big(\frac{B}{\sqrt{\varepsilon}}t\Big) + \frac{1}{B\sqrt{\varepsilon}}\Big[\boldsymbol{q}_0 \times \boldsymbol{B} - \nabla\bar{\Psi}_0\Big] \sin\Big(\frac{B}{\sqrt{\varepsilon}}t\Big),$$

$$\boldsymbol{q} = \boldsymbol{q}_0 + \left[\boldsymbol{j}_0 \frac{\sqrt{\varepsilon}}{B} \sin\Big(\frac{B}{\sqrt{\varepsilon}}t\Big) - \frac{1}{B^2}\big[\boldsymbol{q}_0 \times \boldsymbol{B} - \nabla\bar{\Psi}_0\big]\big[\cos\Big(\frac{B}{\sqrt{\varepsilon}}t\Big) - 1\big]\right] \times \boldsymbol{B},$$

where $\bar{\Psi}_0$ is defined as the solution of:

$$\begin{cases} -\Delta\bar{\Psi}_0 = -\nabla \cdot \big(\boldsymbol{q}_0 \times \boldsymbol{B}\big), \\ \nabla\bar{\Psi}_0 \cdot \boldsymbol{n} = \big(\boldsymbol{q}_0 \times \boldsymbol{B}\big) \cdot \boldsymbol{n}, \qquad \text{on the boundary.} \end{cases} \tag{B.7}$$

Hence, both ion and electron quantities have a periodic behavior with the same angular frequency $B/\sqrt{\varepsilon}$. This unexpected analysis points out the influence of the electroneutrality, since if discarding the divergence free constraint we would obtain oscillations with angular frequency $B$ for the ions, and $B/\varepsilon$ for the electrons. For numerical applications, this means that it is not needed to resolve the electron cyclotronic frequency to obtain accurate approximations of system (B.1).

*Appendix B.2. Projection method*

Following the same lines, we can analyze the projection method for the problem (B.1). First, let us note that the term $(1-\varepsilon)\boldsymbol{j} \times \boldsymbol{B}$ in the right-hand-side of the second equation of (B.1) plays no role in the previous analysis (at least in the derivation of the exact expression for $\boldsymbol{q}$ and $\boldsymbol{j}$). Indeed, in our simplified geometry this term is irrotational (since the current is divergence free) and, consequently, could be included in the definition of the potential $\Psi$. For this reason, in the sequel we introduce an additional coefficient $\mu$ and write the system as follows:

$$\begin{cases} \partial_t \boldsymbol{q} = \boldsymbol{j} \times \boldsymbol{B}, \\ \varepsilon\partial_t \boldsymbol{j} + \nabla\Psi = \Big(\boldsymbol{q} - (1-\mu)\boldsymbol{j}\Big) \times \boldsymbol{B}, \\ \nabla \cdot \boldsymbol{j} = 0. \end{cases} \tag{B.8}$$

The system (B.1) considered previously corresponds to $\mu = \varepsilon$. However, since the solutions $\boldsymbol{j}$ and $\boldsymbol{q}$ of the system (B.8) are the same for any values of $\mu$, for the sake of simplicity we will consider the value $\mu = 1$ at the end of this section.

The projection method starts from the exact initial states $\boldsymbol{q}^0 = \boldsymbol{q}_0$ and $\boldsymbol{j}^0 = \boldsymbol{j}_0$. Then, assuming given the states $\boldsymbol{q}^k$ and $\boldsymbol{j}^k$ at the time $t_k = k\delta t$, the algorithm to define $\boldsymbol{q}^{k+1}$ and $\boldsymbol{j}^{k+1}$ writes in two steps:

- in the first step, we compute predicted quantities $\hat{\boldsymbol{q}}$ and $\hat{\boldsymbol{j}}$ discarding the divergence free constraint, that is we solve the system:

$$\begin{cases} \partial_t \boldsymbol{q} = \boldsymbol{j} \times \boldsymbol{B}, \\ \varepsilon\partial_t \boldsymbol{j} = \Big(\boldsymbol{q} - (1-\mu)\boldsymbol{j}\Big) \times \boldsymbol{B}, \end{cases} \tag{B.9}$$

  on one time step. No boundary condition are needed at this step.

- then, starting from the predicted quantities $\hat{\boldsymbol{q}}$ and $\hat{\boldsymbol{j}}$, we compute the electric potential $\Psi^{k+1}$, the end-of-step current $\boldsymbol{j}^{k+1}$ and total momentum $\boldsymbol{q}^{k+1}$ by solving on one time step:

$$\begin{cases} \partial_t \boldsymbol{q} = 0, \\ \varepsilon \partial_t \boldsymbol{j} + \nabla \Psi = 0, \\ \nabla \cdot \boldsymbol{j} = 0. \end{cases} \tag{B.10}$$

  The boundary condition $\boldsymbol{j} \cdot \boldsymbol{n} = 0$ is enforced at this step.

As in the previous section, these two steps can be written using the variables $\mathrm{d}_{\boldsymbol{j}} = \nabla \cdot \boldsymbol{j}$, $\mathrm{r}_{\boldsymbol{j}} = \nabla \times \boldsymbol{j}$, $\mathrm{d}_{\boldsymbol{q}} = \nabla \cdot \boldsymbol{q}$ and $\mathrm{r}_{\boldsymbol{q}} = \nabla \times \boldsymbol{q}$. The prediction step writes:

$$\begin{cases} \partial_t \mathrm{r}_{\boldsymbol{q}} = -B\ \mathrm{d}_{\boldsymbol{j}}, \qquad \partial_t \mathrm{d}_{\boldsymbol{q}} = B\ \mathrm{r}_{\boldsymbol{j}}, \\ \varepsilon \partial_t \mathrm{r}_{\boldsymbol{j}} = -B \left( \mathrm{d}_{\boldsymbol{q}} - (1-\mu)\mathrm{d}_{\boldsymbol{j}} \right), \qquad \varepsilon \partial_t \mathrm{d}_{\boldsymbol{j}} = B \left( \mathrm{r}_{\boldsymbol{q}} - (1-\mu)\mathrm{r}_{\boldsymbol{j}} \right), \end{cases} \tag{B.11}$$

whereas the correction step writes

$$\partial_t \mathrm{r}_{\boldsymbol{q}} = 0, \qquad \partial_t \mathrm{d}_{\boldsymbol{q}} = 0, \qquad \partial_t \mathrm{r}_{\boldsymbol{j}} = 0, \qquad \mathrm{d}_{\boldsymbol{j}} = 0\,.$$

Thus, the correction step consists of setting $\mathrm{d}_{\boldsymbol{j}}$ to zero while preserving the quantities $\mathrm{r}_{\boldsymbol{q}}$, $\mathrm{d}_{\boldsymbol{q}}$ and $\mathrm{r}_{\boldsymbol{j}}$. It means that if we manage to eliminate $\mathrm{d}_{\boldsymbol{j}}$ from the system (B.11), we will obtain the system effectively solved for $\mathrm{r}_{\boldsymbol{q}}$, $\mathrm{d}_{\boldsymbol{q}}$, and $\mathrm{r}_{\boldsymbol{j}}$ when using the projection method. To this end, we take the time derivative of the equations on $\mathrm{r}_{\boldsymbol{q}}$ and $\mathrm{r}_{\boldsymbol{j}}$, and replace $\partial_t \mathrm{d}_{\boldsymbol{j}}$ by its expression as a function of $\mathrm{r}_{\boldsymbol{q}}$ and $\mathrm{r}_{\boldsymbol{j}}$. Finally, the projection method consists of solving the following system at each time step:

$$\begin{cases} \partial_{tt} \mathrm{r}_{\boldsymbol{q}} = -\dfrac{B^2}{\varepsilon} \Big( \mathrm{r}_{\boldsymbol{q}} - (1-\mu)\mathrm{r}_{\boldsymbol{j}} \Big)\,, \\ \varepsilon \partial_{tt} \mathrm{r}_{\boldsymbol{j}} = -\dfrac{B^2}{\varepsilon} \left( \varepsilon \mathrm{r}_{\boldsymbol{j}} - (1-\mu)\big( \mathrm{r}_{\boldsymbol{q}} - (1-\mu)\mathrm{r}_{\boldsymbol{j}} \big) \right), \\ \partial_t \mathrm{d}_{\boldsymbol{q}} = B\ \mathrm{r}_{\boldsymbol{j}}\,, \\ \mathrm{d}_{\boldsymbol{j}} = 0\,. \end{cases} \tag{B.12}$$

The initial conditions at time $t_k = k\delta t$ associated to this system are defined from the given state $\boldsymbol{j}^k$, $\boldsymbol{q}^k$. Since we have now second order equations in time, it is needed to define initial conditions for $\partial_t \mathrm{r}_{\boldsymbol{q}}$ and $\partial_t \mathrm{r}_{\boldsymbol{j}}$. Because at the beginning of the time step $\mathrm{d}_{\boldsymbol{j}^k}$ is zero, we obtain the following initial conditions from system (B.11):

$$\mathrm{r}_{\boldsymbol{q}}(t_k) = \mathrm{r}_{\boldsymbol{q}^k}, \qquad \mathrm{r}_{\boldsymbol{j}}(t_k) = \mathrm{r}_{\boldsymbol{j}^k}, \qquad \mathrm{d}_{\boldsymbol{q}}(t_k) = \mathrm{d}_{\boldsymbol{q}^k}, \qquad \partial_t \mathrm{r}_{\boldsymbol{q}}(t_k) = 0, \qquad \partial_t \mathrm{r}_{\boldsymbol{j}}(t_k) = -\frac{B}{\varepsilon} \mathrm{d}_{\boldsymbol{q}^k}.$$

This system can be compared to the system (B.3)–(B.6) putting in light the splitting error. First, one observes that, contrarily to what happens for exact solution of (B.8), here the term $(1-\mu)\boldsymbol{j} \times \boldsymbol{B}$ plays a role. Even if the system (B.12) can be explicitly solved in the case where $\mu = \varepsilon$, it is quite cumbersome to carry out the explicit form of the splitting errors in this case. However, we can easily go further if $\mu = 1$, since in this case the system writes:

$$\begin{cases} \partial_{tt} \mathrm{r}_{\boldsymbol{q}} = -\dfrac{B^2}{\varepsilon} \mathrm{r}_{\boldsymbol{q}}\,, \\ \partial_{tt} \mathrm{r}_{\boldsymbol{j}} = -\dfrac{B^2}{\varepsilon} \mathrm{r}_{\boldsymbol{j}}\,, \\ \partial_t \mathrm{d}_{\boldsymbol{q}} = B\ \mathrm{r}_{\boldsymbol{j}}\,, \\ \mathrm{d}_{\boldsymbol{j}} = 0\,. \end{cases}$$

so that, the quantities $\mathrm{r}_{\boldsymbol{j}}$, $\mathrm{d}_{\boldsymbol{q}}$, $\mathrm{d}_{\boldsymbol{j}}$ may be accurately computed, whereas a splitting error is observed on $\mathrm{r}_{\boldsymbol{q}}$:

$$\mathrm{r}_{\boldsymbol{q}^k} = \mathrm{r}_{\boldsymbol{q}_0}\Big[\cos\Big(\frac{B}{\sqrt{\varepsilon}}\delta t\Big)\Big]^k.$$

Thus, for small time step $\delta t$, the splitting error at a given time $T > 0$ behaves like $B^2/(2\varepsilon)T\delta t$. It is of order 1, as expected for the (non incremental) projection method, but more significantly the constant $B^2/(2\varepsilon)$ is in practice large. Because the magnetic field is strong, it turns out that the projection method for system (B.8) leads to an important splitting error even for the very small time step $\delta t = 2\pi\varepsilon/B$, that is associated to the electron cyclotronic period.

**Acknowledgments**

This work has been carried out within the framework of the EUROfusion Consortium and has received funding from the European Union's Horizon 2020 research and innovation program under grant agreement number 633053. The views and opinions expressed herein do not necessarily reflect those of the European Commission. The authors wish to thank T. Goudon for fruitful discussions about the simplified problem discussed in Appendix of this article.

## References

[1] D.V. Anderson, W.A. Cooper, R. Gruber, S. Merazzi, U. Schwenn, TERPSICHORE: A three-dimensional ideal MHD stability program, Scientific Computing on Supercomputers II, Devreese and Van Camp, eds, Plenum Press, NY, 1990.

[2] U.M. Ascher, S.J. Ruuth, R.J. Spiteri, Implicit-explicit Runge-Kutta methods for time-dependent partial differential equations, Appl. Numer. Math., 25:151–167, 1997.

[3] R. Balescu, *Transport processes in plasmas*, North-Holland; Amsterdam (Netherlands), 1988.

[4] X. Bonnin, A.S. Kukushkin, D.P. Coster, Code development for ITER edge modeling - SOLPS5.1, *J. of Nuclear Material*, 390-391, 274-277, 2009.

[5] H. Buffereand, B. Bensiali, J. Bucalossi, G. Ciraolo, P. Genesio, Ph. Ghendrih, Y. Marandet, A. Parades, F. Schwander, E. Serre, P. Tamain, Near wall plasma simulation using penalization technique with the transport code SolEdge2D-Eirene, *J. of Nuclear Material*, 438, 5445-5448, 2013.

[6] J. Blum, C. Boulbe, B. Faugeras, Reconstruction of the equilibrium of the plasma in a Tokamak and identification of the current density profile in real time *J. of Comput. Phys.*, 231, 960-980, 2012.

[7] A. Bonnement, Modélisation numérique par approximation fluide du plasma de bord des tokamaks (projet ITER), PHD thesis, University of Nice-Sophia Antipolis, 2012.

[8] A. Bonnement, S. Minjeaud, R. Pasquetti, Towards a Fourier-SEM solver of fluid models in tokamaks, *Lecture Notes in Computational Science and Engineering : Spectral and High Order Methods for Partial Differential Equations - ICOSAHOM 2012*, 95, Springer, 169-178, 2014. 2012.

[9] S.I. Braginskii, Transport processes in a plasma. Review of Plasma Physics, 1: 205-311, 1965.

[10] C. Canuto, M.Y. Hussaini, A. Quarteroni, Th. Zhang, *Spectral methods: Application to complex geometries and applications to fluid dynamics*, Springer, 2007.

[11] F.F. Chen, *Introduction to plasma physics and controlled fusion. 1. Plasma physics*, New York N.Y. London : Plenum Press cop., 1984.

[12] B.D. Dudson, M.V. Umansky, X.Q. Xu, P.B. Snyder, H.R. Wilson, BOUT++: A framework for parallel plasma fluid simulations, *Computer Physics Communications*, 180, 1467-1480, 2007.

[13] B. van Es, B. Koren, H. de Blank, J. Hugo, Finite-difference schemes for anisotropic diffusion, *J. Comput. Phys.*, 272, 526-549, 2014.

[14] S. Günter, Q. Yu, J. Krüger, K. Lackner, Modelling of heat transport in magnetised plasmas using non-aligned coordinates, *J. of Comput. Phys.*, 209, 354-370, 2005.

[15] O. Czarny, G.T.A. Huysmans, MHD stability in x-point geometry : simulation of ELMS, Nuclear fusion, 47:659-666, 2007.

[16] J.L. Delcroix, A. Bers, Physique des plasmas (II), InterEditions, / CNRS Editions, 1994.

[17] M.O. Deville, P.F. Fischer, E.H. Mund, *High-order methods for incompressible flows*, Cambridge University Press, 2002.

[18] E.M. Epperlein, M.G. Haines, Plasma transport coefficients in a magnetic field by direct numerical simulation of the Fokker-Planck equation, *Phys. Fluids*, 29 (4), 1029-1041, 1986.

[19] V. Grandgirard, Y. Sarazin, X. Garbet, G. Dif-Pradalier, P. Ghendrih, N. Crouseilles, G. Latu, E. Sonnendrücker, N. Besse, P. Bertrand, GYSELA, a full-f global gyrokinetic Semi-Lagrangian code for ITG turbulence simulations, *Proceedings of Theory of Fusion Plasmas*, Varenna, 2006.

[20] J.L. Guermond, P. Minev, J. Shen, An overview of projection methods for incompressible flows, *Comput. Methods Appl.Mech. Engrg.*, 165, 6011- 6045, 2006.

[21] J.D. Huba, *NRL Plasma formulary*, The office of naval research, Washington DC, 2009.

[22] L. Isoardi, G. Chiavassa, G. Ciraolo, P. Haldenwang, E. Serre, Ph. Ghendrih, Y. Sarazin, F. Schwander, P. Tamain, Penalization modeling of a limiter in the tokamak edge plasma, *J. Comput. Phys.* 229, 2220-2235, 2010

[23] S. Jardin, *Computational methods in plasma physics*, Chapman & Hall / CRC, 2010

[24] G.E. Karniadakis, S.J. Sherwin, *Spectral hp element methods for CFD*, Oxford Univ. Press, London, 1999.

[25] P.J. Knight, A. Thyaragaja, T.D. Edwards, J. Hein, M. Romanelli, K.G. McClements, CENTORI: A global toroidal electromagnetic two-fluid plasma turbulence code, *Computer Physics Communications*, 183, 2346-2363, 2012.

[26] L. Lazar, R. Pasquetti, F. Rapetti, Fekete-Gauss spectral elements for incompressible Navier-Stokes flows: The two-dimensional case, *Comm. in Comput. Phys.*, 13, 1309-1329, 2013.

[27] J. Loizu, P. Ricci, F. D. Halpern, S. Jolliet, Boundary conditions for plasma fluid models at the magnetic presheath entrance, *Physics of plasmas*, 19 , 122307, 2012.

[28] H. Lütjens, J.F. Luciani, The XTOR code for nonlinear 3D simulations of MHD instabilities in tokamak plasmas, *J. Comput. Phys.*, 227, 6944-6966, 2008.

[29] E.T. Meier, U. Shumlak, A general nonlinear fluid model for reacting plasma-neutral mixtures, *Physics of Plasmas*, 19, 072508, 2012.

[30] M. Melenk, On condition numbers in hp-FEM with Gauss- Lobatto based shape functions, *J. of Comp. and Appl. Math.*, 139, 21-48, 2002.

[31] S. Minjeaud, R. Pasquetti, High order approximation of a tokamak edge plasma transport minimal model with Bohm boundary conditions, *J. of Comput. Phys.* , 285, 84-87, 2015.

[32] C. Michoski, D. Meyerson, T. Isaac, F. Waelbroeck, Discontinuous Galerkin methods for plasma physics in the scrape-off layer of tokamaks, *J. of Comput. Phys.* , 274, 898-919, 2014.

[33] P. Ricci, F.D. Halpern, S. Jolliet, J. Loizu, A. Mosetto, A. Fasoli, I. Furno, C. Theiler, Simulation of plasma turbulence in the scrape-off layer conditions: the GBS code, simulation results and code validation, *plasma Phys. Control. Fusion*, 54, 124047, 2012.

[34] U. Shumlak, R. Lilly, N. Reddell, E. Sousa, B. Srinivasan, Advanced physics calculations using a multi-fluid plasma model, *Computer Physics Communications*, 182, 1767-1770, 2011.

[35] P. C Stangeby, *The plasma boundary of magnetic fusion devices*, New York : Taylor & Francis cop. 2000.

[36] P. Tamain, Ph. Ghendrih, E. Tsitrone, V. Grandgirard, X. Garbet, Y. Sarazin, E. Serre, G. Ciraolo, G. Chiavassa, Tokam-3d: A fluid code for tranport and turbulence in the edge plasma of tokamaks, *J. of Comput. Phys.*, 229(2), 361-378, 2010.

[37] C.J. Xu, R. Pasquetti, Stabilized spectral element computations of high-Reynolds number incompressible flows, *J. of Comput. Phys.*, 196/2, pp. 680-704, 2004.